

A frequentist view on the two-body decaying dark matter model

Thomas Montandon,¹ Elsa M. Teixeira,¹ Adèle Poudou,¹ and Vivian Poulin¹

¹*Laboratoire Univers & Particules de Montpellier,
CNRS & Université de Montpellier (UMR-5299), 34095 Montpellier, France**

Decaying dark matter (DDM) has emerged as an interesting framework to extend the Λ -cold-dark-matter (Λ CDM) model, as many particle physics models predict that dark matter may not be stable over cosmic time and can impact structure formation. In particular, a model in which DM decays at a rate Γ and imprints a velocity kick v onto its decay products leads to a low amplitude of fluctuations, as quantified by the parameter S_8 , in better agreement with that measured by some past weak lensing surveys. Bayesian analyses have provided mixed conclusions regarding its viability, with a reconstructed clustering amplitude only slightly below the standard Λ CDM value. In this paper, we contrast previous results with a frequentist analysis of Planck and SDSS BAO data. We find that the 68% confidence level region corresponds to a decay half-life of $6.93^{+7.88}_{-2.85}$ Gyr and a velocity kick of 1250^{+1450}_{-1000} km/s. These 1σ constraints strongly differ from their Bayesian counterparts, indicating the presence of volume effect in the Bayesian analysis. Moreover, we find that under the DDM model, the frequentist analysis predicts lower values of S_8 , in agreement with those found by KiDS-1000 and DES-Y3 at $\sim 1.5\sigma$. We further show that previously derived KiDS-1000 constraints that appeared to exclude the best-fit model from *Planck* data were driven by priors on the primordial amplitude A_s and spectral index n_s . When those are removed from the analysis, KiDS-1000 constraints on the DDM parameters are fully relaxed. It is only when applying *Planck*-informed priors on A_s and n_s to the KiDS-1000 analysis that one can constrain the model. We further highlight that in the absence of such priors, the region of scales best-measured by KiDS-1000 does not exactly match the S_8 kernel (centred around $k \sim 0.1 h/\text{Mpc}$), but rather a slightly smaller range of scales centred around $k \sim 0.3 h/\text{Mpc}$. One must thus be careful in applying S_8 constraints to a model instead of the full data likelihood.

I. INTRODUCTION

Over the past decades, the Λ CDM (“Lambda” Cold Dark Matter) cosmological model has emerged as the standard paradigm for describing the Universe, providing an excellent fit to a wide range of observations spanning both early and late cosmic times. From the precise measurements of the Cosmic Microwave Background (CMB) and Big Bang Nucleosynthesis (BBN) to large-scale structure surveys, baryon acoustic oscillations (BAO), and supernovae type Ia (SNIa), the Λ CDM framework has proven remarkably successful. Nonetheless, despite its empirical success, the fundamental nature of its dominant constituents – cold dark matter (CDM) and dark energy (Λ) – remains unknown, and tensions have emerged as the precision of cosmological data has improved.

Among the most prominent of these discrepancies is the so-called S_8 tension, referring to the $2 - 3\sigma$ disagreement between the amplitude of matter fluctuations inferred from high-redshift CMB data and direct measurements at low redshift from weak lensing (WL) surveys. The parameter $S_8 = \sigma_8 \sqrt{\Omega_m}/0.3$, where σ_8 quantifies the matter fluctuation amplitude on $8 h^{-1}\text{Mpc}$ scales and Ω_m the total matter density, encapsulates this tension under Λ CDM. For instance, the *Planck* satellite has measured $S_8 = 0.825 \pm 0.011$ [1], while weak lensing surveys like the Kilo-Degree Survey (KiDS) [2, 3], the

Dark Energy Survey (DES) [4], and the Hyper Supreme-Cam (HSC) [5] measure consistently lower values, such as $S_8 = 0.748^{+0.021}_{-0.025}$ in KiDS-1000 [6]. However, more recent analyses such as DES-Y3 [7] and the KiDS-Legacy results [8] strongly mitigate the existence of a S_8 tension. The large constraining power of weak lensing will be vastly used by the Vera Rubin observatory [9], *Euclid* [10], Nancy Grace Roman Space Telescope [11] and the Chinese Space Station Telescope [12]. Hence, we should expect definitive answers regarding small-scale physics in the next few years. However, whether or not there is an S_8 tension, constraining physically motivated models remains crucial, given that the nature of CDM is still entirely unknown.

While an S_8 tension might also emerge from small-scale physics such as baryonic feedback or nonlinear structure formation [13–15], it could also point to the need for new physics beyond the standard model. Among the many proposed extensions to Λ CDM, a particularly well-motivated class involves modifying the properties of dark matter itself, see *e.g.* Refs. [16–20] for recent models. In this context, decaying dark matter (DDM) scenarios [21–24] have received growing attention [25–29], as they can naturally predict a suppression of power on small scales ($k \sim 0.1 - 1 h/\text{Mpc}$), thereby alleviating the S_8 tension.

Many particle physics-motivated scenarios of dark matter [30–37] question its stability on cosmological timescales and can effectively be described by a two-body DDM model. While the DDM framework has attracted attention for its potential to ease the S_8 tension, disfavoring it – as suggested by recent weak lensing measure-

* thomas.montandon@umontpellier.fr

ments from DES-Y3 [7] and KiDS-Legacy [8] – would have broader implications, potentially ruling out a wide class of unstable dark matter models.

The most simple class of DDM considers the decay of CDM into dark radiation, for which strong constraints can be obtained with CDM data [29, 38–40]. Another kind of interesting variant is the two-body decaying dark matter model (DDM) [41], in which a fraction of the CDM decays into a massive daughter particle and a massless component (*e.g.* dark radiation). The massive product inherits a velocity kick from energy-momentum conservation, leading to a scale-dependent suppression of the matter power spectrum due to its free-streaming. This mechanism can alter structure formation like warm dark matter, but with a redshift and scale dependence that can leave the early time unchanged compared to CDM.

Previous studies have investigated the phenomenology of the DDM model using linear perturbation theory [24, 41] or simulations [42, 43]. Constraints have been performed using the *Planck* CMB data, BAO and supernova [24], BOSS full shape [40], Milky Way satellite counts [44], and Lyman- α forest observations [45, 46]. More recently, Ref. [29] used the weak lensing survey KiDS-1000 to derive the strongest constraints obtained. As far as the two-body decay is concerned – see Ref. [39] for a profile likelihood analysis of the DDM model decaying into radiation – all these studies have used the standard Bayesian framework which is known to be affected by prior volume effects [47].

In this work, we further explore the DDM scenario in light of the latest cosmological observations. We perform an independent analysis of KiDS-1000 cosmic shear data using a nonlinear matter power spectrum emulator developed in Ref. [29], and reanalyse the *Planck* 2018 CMB data, adding also BAO and supernovae, to extract updated constraints using a frequentist analysis to get rid of any prior volume effects. We also combine both datasets using *Planck* informed priors to assess the potential of this scenario to reconcile CMB and WL observations.

This paper is structured as follows: Section II introduces the DDM model, the dataset and the methodology used. In Section III, we present the standard Bayesian results and the *Planck* likelihood profiles analysis. Section IV discusses the constraints of KiDS-1000 and proposes a consistent KiDS-1000 and *Planck* joint analysis. The conclusions are presented in Section V.

II. MODEL AND METHODOLOGY

The standard cosmological model, flat Λ CDM, is characterised by a set of fundamental parameters describing the evolution, composition and initial conditions of the Universe. These include the Hubble constant H_0 , the cold dark matter density parameter Ω_c , the baryon energy density Ω_b , and the photon energy density, which is now well constrained through the monopole temperature of the CMB, measured to be $T_0 = 2.7255 \pm 0.0006$ K [48].

Motivated by single-field inflation models, the primordial initial conditions are assumed to be Gaussian and adiabatic perturbations, with a power spectrum following a power law with amplitude A_s and spectral index $n_s - 1$.

We now focus on the scenario where CDM particles are unstable and can decay into a lighter particle and a massless relativistic particle.

A. Two-Body Decaying Dark Matter

In this work, we focus on the DDM model in which a CDM particle of mass M_{CDM} decays into two lighter particles: a massive “warm” daughter particle of mass M_{WDM} and a massless relativistic particle. The decay is characterised by the decay rate Γ , which is inversely proportional to the particle’s lifetime. The warm daughter particle inherits a velocity kick v . Given by the kinematic relation of the decay, the fraction ϵ of rest-mass energy of the mother particle converted into kinetic energy reads:

$$\epsilon = \frac{1}{2} \left(1 - \frac{M_{\text{WDM}}^2}{M_{\text{CDM}}^2} \right). \quad (1)$$

In the non-relativistic limit, the velocity kick is given by $v = \epsilon c$. A third parameter, f , represents the fraction of unstable CDM that decays into WDM. In this analysis, we focus on the case $f = 1$, where all the CDM decays into WDM. A thorough account of the phenomenology of this model and the corresponding set of dynamical equations are presented in Refs. [24, 49].

Note that the Λ CDM limit is recovered when the decay lifetime greatly exceeds the age of the Universe ($\Gamma^{-1} \rightarrow \infty$) or when the momentum transfer is negligible ($\epsilon \rightarrow 0$), leaving the daughter particle effectively cold. The limit $\epsilon \rightarrow 0.5$ ($M_{\text{WDM}} \rightarrow 0$) corresponds to a one-body decay with the daughter particle acting effectively as dark radiation.

The momentum transfer to the daughter particle generates a time- and scale-dependent free-streaming scale. Below this scale, density perturbations are suppressed because the pressure of the warm daughter particle counteracts gravitational collapse. The time dependence of this effect is governed by the dark matter lifetime $\sim \Gamma^{-1}$, such that only perturbation modes below the free-streaming scale are significantly affected after times $t > \Gamma^{-1}$. Consequently, perturbations evolve similarly to those of standard CDM for times $t < \Gamma^{-1}$ and on scales larger than the free-streaming scale. This allows the model to reproduce the CMB temperature, polarisation and lensing anisotropies with a CDM-like behaviour while still reducing small-scale power in the late-time matter power spectrum due to the suppression of growth at small scales. The depth and the scale of the matter power suppression are controlled by Γ and v , respectively.

The growth of cosmic structures is often quantified by the variance of matter fluctuations smoothed over a scale

r , defined as:

$$\sigma_r^2 = \int_0^\infty \frac{k^2 dk}{2\pi^2} P_m(k) W^2(r, k), \quad (2)$$

where W is the Fourier transform of a top-hat filter, k is the corresponding wavenumber in Fourier space and $P_m(k)$ is the matter power spectrum:

$$\langle \delta_m(\mathbf{k}_1) \delta_m(\mathbf{k}_2) \rangle = (2\pi)^3 \delta^D(\mathbf{k}_1 + \mathbf{k}_2) P_m(k_1), \quad (3)$$

where δ_m is the total matter density contrast, and δ^D is the Dirac-delta function. The characteristic scale of cosmic-structure formation is usually taken to be $r \sim 8h^{-1}$ Mpc, in which case we refer to σ_8 in Eq. (2). The key signature of the warm dark matter species is to predict a smaller value of σ_8 than CDM. However, weak lensing measurements are sensitive to both the amplitude of matter fluctuations, σ_8 , and the total matter density, Ω_m , leading to a degeneracy between these parameters. This motivates the use of the derived parameter

$$S_8 = \sigma_8 \sqrt{\frac{\Omega_m}{0.3}}. \quad (4)$$

The linear evolution of the DDM model has been implemented in the Einstein-Boltzmann solver CLASS [50, 51] and made publicly available [24]. This allows efficient numerical computation of the linear power spectrum and the CMB angular power spectra C_ℓ :

$$\langle a_{\ell_1 m_1}^X a_{\ell_2 m_2}^Y \rangle = \delta_{\ell_1 \ell_2}^K \delta_{m_1 m_2}^K C_{\ell_1}^{XY}, \quad (5)$$

where δ^K is the Kronecker-delta, and X, Y denote temperature, polarisation, or lensing fields.

For late-time probes, such as the case of galaxy weak lensing, which we will consider, nonlinear corrections are required. The nonlinear matter power spectrum is often computed using Halofit [52, 53], calibrated on Λ CDM simulations. DDM N-body simulations have been performed in Ref. [43]. Here, the latest nonlinear power spectrum emulation of Ref. [29] is employed. Their emulator, DMemu [29], provides the nonlinear suppression factor:

$$P_{\text{NL}}^{\text{ADDM}}(k, z) = P_{\text{NL}}^{\Lambda\text{CDM}}(k, z) \times S^{\Gamma, v}(k, z). \quad (6)$$

A significant source of potential degeneracies is baryonic effects, which also affect small-scale power, necessitating careful modelling [54]. To include them, we use the same methodology as in Ref. [55], which consists of marginalising over the baryonic feedback parameter using HMcode2020 [56].

The cosmic shear angular power spectrum, computed using the Limber approximation [57], is given by:

$$C_\ell^{(ij)} = \int_0^{\chi_h} \frac{d\chi}{\chi^2} W_\Phi^{(i)}(\chi) W_\Phi^{(j)}(\chi) P_{\text{NL}} \left(\frac{\ell + 1/2}{\chi}, z(\chi) \right), \quad (7)$$

where χ_h is the comoving horizon distance, and $W_\Phi^{(i)}$ is the lensing kernel of the tomographic bin (i). For details on intrinsic alignment modelling, see Ref. [58].

B. Datasets and Methodology

In this work, we use two datasets labelled “*Planck*” and “KiDS-1000”.

- *Planck* refers to the standard *Planck* CMB data compiled in the Plik 2018 likelihood [59], including high- and low- ℓ temperature, polarisation, and cross-correlations, as well as lensing [60]. In addition, we include the BAO measurements from the low-redshift surveys 6dFGS [61] and SDSS DR7 [62], as well as the full BOSS DR12 [63]. Finally, we include the Pantheon-Plus compilation of Type Ia supernovae distance moduli measurements [64].
- the Kilo-Degree Survey KiDS-1000 [57], also labeled as “KiDS”, is a galaxy catalog providing information about ~ 20 million galaxies divided into 5 redshift bins covering a range of $z \in [0.1, 1.2]$. The catalogue is analysed by the European Southern Observatory with the Very Large Telescope (VLT). We use the likelihood COSEBIs [65–67].¹

To analyse these two datasets within the theoretical framework of Section II A, we first perform a Bayesian analysis using the standard Markov Chain Monte Carlo (MCMC) method [68, 69]. For the *Planck* analysis, we use MontePython [70, 71]. For practical reasons, we use CosmoSIS [72], which directly includes the COSEBIs likelihood, as well as more recent likelihoods such as DES-Y3 [7], and their joint analysis [55] which will be used in future works. We vary all 6- Λ CDM parameters within large flat priors. This is particularly important for A_s and n_s , as we show later on. The DDM parameters are varied within log-flat priors in the *Planck* analysis:

$$\begin{aligned} \log_{10} \Gamma \times \text{Gyr} &\in [-4, 1], \\ \log_{10} v \times \text{s/km} &\in [1.5, 5]. \end{aligned} \quad (8)$$

For KiDS-1000, we restrict the priors to

$$\begin{aligned} \log_{10} \Gamma \times \text{Gyr} &\in [-4, -1.13], \\ \log_{10} v \times \text{s/km} &\in [1.5, 3.7], \end{aligned} \quad (9)$$

to match the regime of validity of the emulator in Eq. (6).

Bayesian analyses can suffer from strong prior dependence. Even though the intrinsic interpretation of Bayesian and frequentist approaches differ and cannot strictly be compared, frequentist analyses provide prior-independent constraints that help disentangle the impact

¹ Short before submission of this paper, the last data release was performed under the name KiDS-Legacy [8].

of the priors from that of the likelihood in Bayesian inferences.

To that end, frequentist analyses employ the ‘‘profile likelihood’’ method. Instead of marginalising over nuisance parameters as in Bayesian MCMC, the profile likelihood for a parameter set α is defined as:

$$\mathcal{L}_p(\alpha) = \max_{\theta} \mathcal{L}(\alpha, \theta), \quad (10)$$

where $\mathcal{L}(\alpha, \theta)$ is the full likelihood function, θ represents all parameters to be minimised and α the subset of parameter to study. In our specific case, the parameters of interest are $\alpha \in \{\Gamma, v, \{\Gamma, v\}\}$, while θ includes all remaining cosmological and nuisance parameters over which the likelihood is maximised. For Gaussian likelihoods, we have $-2\log \mathcal{L}_p(\alpha) = \chi_{\alpha}^2$ which allows us to determine confidence intervals from $\Delta\chi^2(\alpha) = \chi^2(\alpha) - \chi_{\text{DDM}}^2$ where χ_{DDM}^2 here represents the global maximum likelihood of the DDM model, hence taking α also as free parameter. To compare the improvement of a model with respect to a reference model – here Λ CDM – we compare their global minima $\Delta\chi_{\text{DDM}}^2 = \chi_{\text{DDM}}^2 - \chi_{\text{CDM}}^2$. We minimise using a simulated annealing method described in Ref. [73].

III. BAYESIAN VS FREQUENTIST ANALYSES

A. Bayesian constraints from *Planck* and KiDS-1000

In Fig. 1, we reproduce the standard Bayesian analysis for ADDM and Λ CDM using the two aforementioned data sets. We show the 2D marginalised posteriors for relevant parameters in the two models: DDM in blue and red, for KiDS-1000 and *Planck*, respectively, and grey and green for the standard Λ CDM model for KiDS-1000 and *Planck*, respectively. In agreement with what has been discussed in past literature, *e.g.* Ref. [29, 57], we can see how KiDS-1000, as well as *Planck*, independently provide precise measurements of S_8 . Famously, the so-called S_8 tension appears as a $\sim 2\sigma$ discrepancy between *Planck* and KiDS-1000 for the Λ CDM model. In that regard, the DDM model helps decrease the tension by extending the 2σ *Planck* contour toward the low- S_8 KiDS-1000 contours. This apparently small improvement should be taken with caution because the DDM parameter space is not well constrained and can, therefore, be subject to a significant volume effect that alters the reconstructed posteriors in a Bayesian analysis. Moreover, as mentioned in the introduction, more recent data such as the DES-Y3 [7] and the KiDS-Legacy results [8] do not show any tension between these two datasets. What we see here is, therefore, likely due to systematic effects in the KiDS-1000 analysis pipeline (see [74] for details).

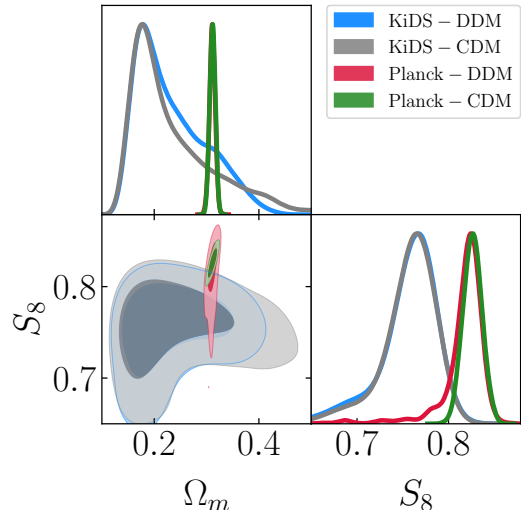


FIG. 1. Constraints on the cosmological parameters S_8 and Ω_m from KiDS-1000 and *Planck* data for both the Decaying Dark Matter (DDM) and Cold Dark Matter (CDM) models. The contours show the 1σ and 2σ confidence regions. This comparison highlights the impact of the DDM model on bringing large-scale structure constraints into closer agreement with *Planck*.

B. Planck Profile Likelihood

We now compute the 1- and 2-dimensional profile likelihood of the two additional parameters of the DDM model Γ and v for the *Planck* data set and discuss their consistency with the KiDS-1000 measurements of S_8 . We focus in the main text on the case of *Planck* data because we have found that the KiDS-1000 profile is strongly affected by the boundary set to one of the nuisance parameters, making difficult the interpretation of the frequentist analysis of KiDS-1000. Concretely, the galaxy intrinsic alignment model parameters (*i.e.* the intrinsic alignment redshift dependence α_1 in CosmoSIS and η_1 in Ref. [55]) seems inconsistent between KiDS-1000 or DES-Y3 compared to direct observation, see footnote 36 in Ref. [55]. A flat prior is adopted on this parameter, making it reach the boundaries during the minimisation procedure, potentially spoiling the results, which at the same time reach the upper bound of the prior on v . We present this analysis in Appendix A and focus here on the case of *Planck*.

We first run a global minimisation and find a global improvement of the DDM fit compared to Λ CDM of

$$\Delta\chi_{\text{Planck,DDM}}^2 = -2.66, \quad (11)$$

corresponding to values

$$\Gamma = 0.10 \text{ Gyr}^{-1}, \quad v = 1250 \text{ km/s}, \quad S_8 = 0.70. \quad (12)$$

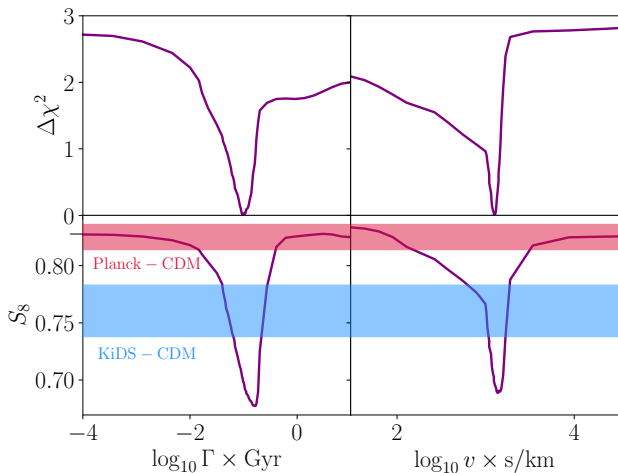


FIG. 2. Planck profile likelihood as a function of $\log_{10} \Gamma$ on the left column and $\log_{10} v$ on the right column. The top panels show $\Delta\chi^2$ while the bottom panels show the S_8 associated with the best-fit. The red band indicates the *Planck* 2018 constraints on S_8 from Ref. [1], while the blue bands indicate the KiDS-1000 constraints from Ref. [57].

Interestingly, this value of S_8 lies at the edge of the Bayesian posterior reconstructed from the analysis of *Planck* data (from Fig. 1 we obtain $S_8 = 0.816 \pm 0.028$), indicating the presence of a significant volume effect as anticipated. In fact, it is even below the interval measured by KiDS-1000. Computing the profile likelihood will thus allow us to derive prior-independent confidence intervals and robustly establish the extent to which the DDM model can reduce S_8 and fit both *Planck* and KiDS-1000 data.

1. 1-dimensional profile

In Fig. 2, we show the profile likelihood as a function of Γ and v on the first and second columns, respectively, by using Eq. (10). The top and bottom panels show respectively the $\Delta\chi^2$ and the derived parameter S_8 computed at the maximum likelihood θ_{\max} . We show the reconstructed value of S_8 in the KiDS-1000 analysis as a blue band and the *Planck* Λ CDM S_8 prediction as a red band in the bottom panels of Fig. 2. Confidence intervals can be extracted from the profile using the Neyman construction [76], which for 1D profile amounts to computing $\Delta\chi^2 < 1$ (4) at 68% (95%) C.L. This procedure yields

$$\begin{aligned} \Gamma &= 0.10^{+0.17}_{-0.05} \text{ Gyr}^{-1}, \\ t_{1/2}^{\text{DDM}} &= 6.93^{+7.88}_{-2.85} \text{ Gyr}, \\ N_0^{\text{DDM}}/N_{\text{ini}} &= 0.25^{+0.27}_{-0.16}, \\ v &= 1250^{+1450}_{-1000} \text{ km/s}, \end{aligned} \quad (13)$$

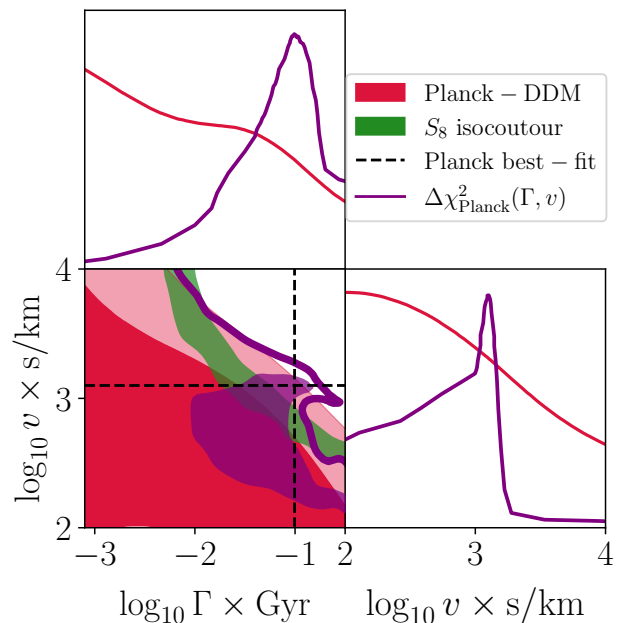


FIG. 3. Constraints on the two additional parameters of the DDM model for *Planck*. The red contours show the result of the Bayesian analysis. The violet line shows the profile likelihood 2σ region, while the filled violet contour represents the 1σ confidence level. The green band represent the S_8 isocontour for the upper and lower bounds of KiDS-1000 [75].

where we have defined $t_{1/2}^{\text{DDM}}$ to be the half-life of DDM and N_0^{DDM} and N_{ini} are respectively the present and initial number of DDM particles. Interestingly, rather than exclusion, the profile likelihood suggests that a specific region of values of Γ and v is weakly favoured over the Λ CDM model, although the Λ CDM limit is obtained at 1.6σ . Hence, our best-fit and 68% credible interval give us a half-life of ~ 7 Gyr, which means that $\sim 75\%$ of the initial DDM particles would have already decayed today. We anticipate that including information from the full shape galaxy power spectrum would alter those constraints, see *e.g.* Ref. [40], and we leave a dedicated combined analysis for future work.

Since low values of Γ indicate a large lifetime compared to the age of the Universe while low v suggests that the decay products remain cold, we trivially recover in these two limits the CDM case and its S_8 Λ CDM value. For too large values of Γ or v , corresponding to either quick decays or hot decay products, the Λ CDM limit is also recovered: the algorithm simply adjusts whichever decay parameter is allowed to freely vary to its CDM limit to prevent a degradation of the fit. Consequently, one recovers again the Λ CDM value of S_8 . Importantly, one can see that the KiDS-1000 S_8 band corresponds to consistently better χ^2 values than the *Planck* Λ CDM S_8 band. This suggests that the DDM model can indeed accommodate the low S_8 value measured by KiDS-1000 despite the apparent Bayesian constraints.

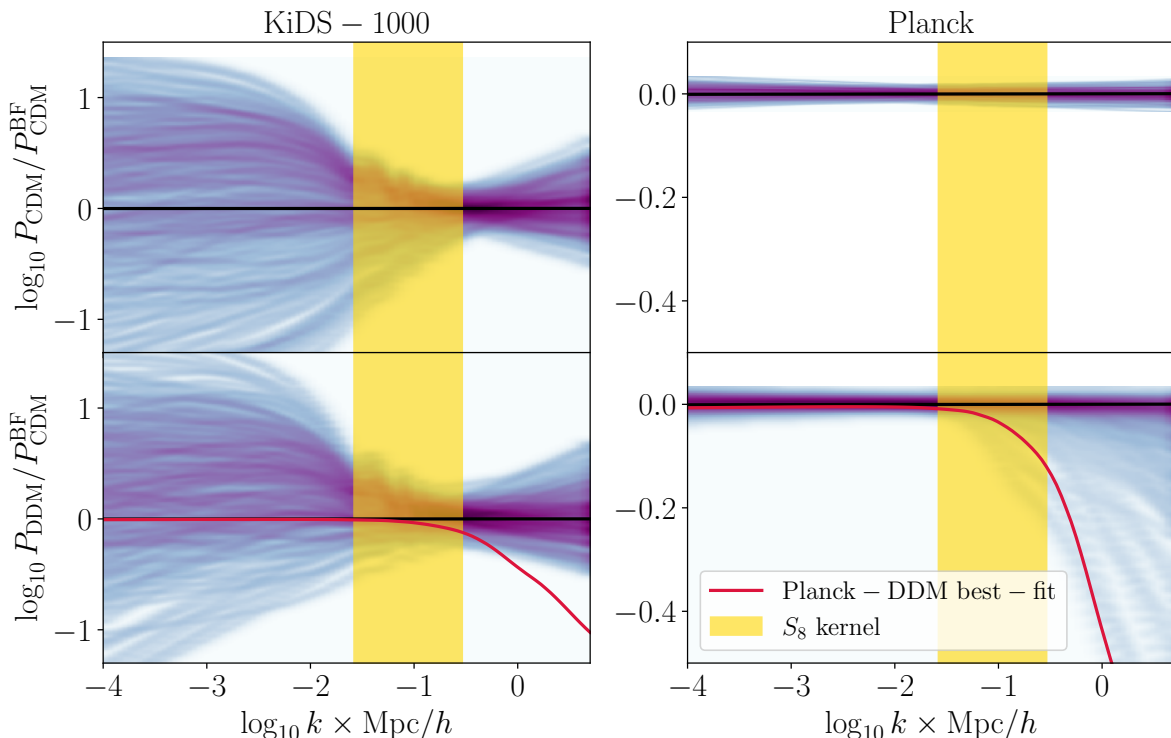


FIG. 4. Power spectrum density normalised to the CDM best-fit of *Planck*. In the left (right) panels for KiDS-1000 (*Planck*), and in the first (second) row for the CDM (DDM) model. The red curve shows the *Planck* maximum likelihood power spectrum with the DDM model. The yellow band represents the main support of the S_8 kernel defined as $W(8h/\text{Mpc}, k) > 0.1$, see Eq. (2).

2. 2-dimensional profile

We show in Fig. 3 the comparison between Bayesian and frequentist intervals reconstructed from the analysis of *Planck* data in the 2-dimensional $\{\log_{10} \Gamma, \log_{10} v\}$ plane, as well as in the 1-dimensional case for each parameter. In the frequentist case, shown in purple, we display the 2-dimensional confidence intervals derived with the Neyman construction at 1σ ($\Delta\chi^2 = 2.3$) and 2σ ($\Delta\chi^2 = 6.17$) and the 1-dimensional profile of Fig. 2 normalised to unity. The marginalised Bayesian posteriors reconstructed from *Planck* are instead shown in red and are similar to those presented in Refs. [29, 77]. In green, we show the isocontours of S_8 for the lower and upper limits of the KiDS-1000 measurements $S_8^{\text{KiDS}} = 0.759^{+0.024}_{-0.021}$, similar to the blue band of Fig. 2. The global minimum is highlighted with the black dashed line, and we recall that it is associated with a low value of $S_8 = 0.70$, according to Eq. (12).

First and foremost, one can see that the 1σ confidence intervals differ from their Bayesian counterparts, confirming the presence of a volume effect. The frequentist interval reveals a closed contour at 1σ , indicating a slight preference for a specific DDM parameter region within *Planck* data. However, the improvement in the fit is too small to overcome the large prior volume, disfavoring the DDM model in the Bayesian analysis. This is similar to

what was found in Ref. [39] in a decaying dark matter model with massless decay products.

Second, it is striking that the S_8 values reconstructed from the KiDS-1000 analysis (green band) intersect the 1σ confidence interval. This confirms that *Planck* data can indeed accommodate a low S_8 value within the DDM model at 1σ . Note also that the confidence intervals follow the Bayesian contours at 2σ , indicating that volume effects are negligible at that level and that the 2σ constraints are robust.

IV. KIDS-1000 ANALYSIS

A. What KiDS-1000 Actually Measures

To better understand the origin of the data constraining power and the S_8 tension, we show in Fig. 4 the constraints to the matter power spectrum obtained with the KiDS-1000 weak lensing survey (left panels) and the *Planck* CMB survey (right panels). There, we have computed the power spectra of 500 random points in the CDM (upper panels) and DDM (lower panels) models taken from their respective MCMC chains and plotted the density of points, all normalised to the best-fit Λ CDM model. In red, we also show the best-fit to *Planck* data in the DDM model. We can, therefore, see the Bayesian

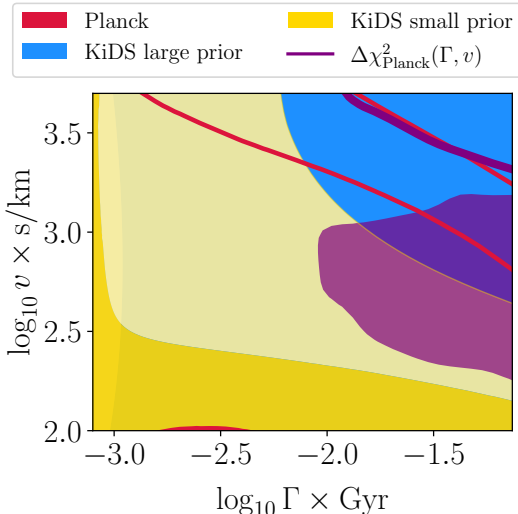


FIG. 5. Bayesian constraints on the DDM model for KiDS-1000 by changing the prior bounds on the primordial amplitude A_s and the spectral index n_s . We also report the *Planck* Bayesian constraints and profile likelihood in red and purple as in Fig. 3 for comparison.

constraints on the matter power spectrum for each scale directly by eye. The yellow band represents the main support of the σ_8 kernel $W(8 \text{ h/Mpc}, k) > 0.1$. The power spectra with less power in this region correspond to a lower S_8 value.

This figure is instructive in several ways: first, it shows that, for *Planck* and in the CDM case (top right panel), the power spectrum is highly constrained at all scales at a $\sim 1\%$ level. However, a large power suppression is allowed in the DDM model (bottom right panel), starting precisely around the S_8 kernel and extending to smaller scales. In that sense, the DDM model can alleviate the S_8 tension: it reduces S_8 without spoiling the fit to the CMB. However, one can see that the largest density of points reconstructed in a Bayesian analysis remains compatible with Λ CDM and no suppression. However, the best-fit to *Planck* data in the DDM model lies on the edge of the point density region, another illustration of the prior volume effect we studied.

Second, it is apparent that KiDS-1000 data only constrain a range of small scales close to the S_8 band. However, the S_8 band does not perfectly overlap with the region of highest density of points and strongest constraints. In fact, it appears that KiDS-1000 data would better constrain a kernel centred around $k \sim 0.5 \text{ Mpc/h}$. The data lacks effective constraining power at large scales, and the constraints are independent of the model (DDM or CDM). This explains why the reconstructed S_8 value in Fig. 1 remains consistent across both models. A power suppression within the DDM model is degenerate with changes in A_s and n_s ; thus, opening up the DDM parameter space does not significantly affect the reconstructed matter power spectrum. Moreover,

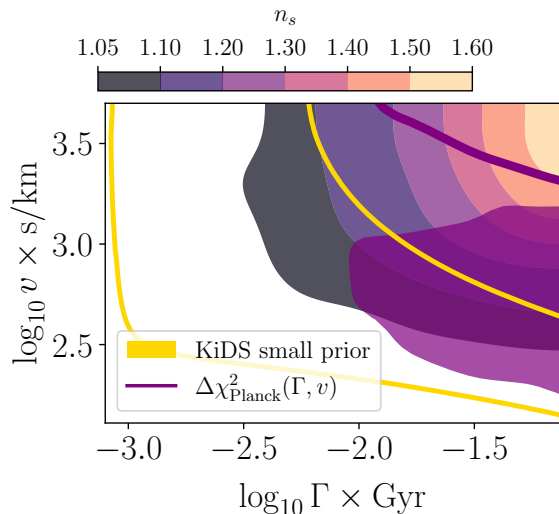


FIG. 6. Smoothed 3D projection of the KiDS-1000 posterior with large priors on A_s and n_s in the Γ - v plane, with the colour mapping representing the inferred scalar spectral index n_s . The yellow contour shows the posterior distribution from KiDS-1000 with small priors for comparison. The purple contours show the results of the *Planck* profile likelihood. This figure illustrates the correlation between n_s and the first diagonal in the plane Γ - v that leads to the constraints presented in Ref. [29].

this suggests that constraints “from KiDS-1000 alone” on the DDM model are prior dependent and that in the absence of any priors on A_s and n_s , this data set does not significantly constrain the DDM model. This will be demonstrated explicitly in the next section. To break the degeneracy between all parameters in the DDM model, one needs to combine observations that probe all scales, *e.g.*, combining *Planck* constraints to A_s and n_s with KiDS-1000.

B. Prior Dependence of KiDS-1000 Constraints

In Fig. 5 we show the reconstructed Bayesian posteriors from the analysis of KiDS-1000 data alone in the $\{\log_{10} \Gamma, \log_{10} v\}$ plane. To illustrate the importance of the priors set on A_s and n_s for the constraints derived on the DDM parameters, we show results for two different sets of priors, given in Table I. The smaller prior range

Parameter	Large prior	Small prior
n_s	$U(0.5, 2)$	$U(0.87, 1.07)$
$10^9 A_s$	$U(0.1, 23.7)$	$U(0.5, 5)$

TABLE I. Priors on A_s and n_s set in the analysis of KiDS-1000 data for the DDM model.

is similar to that used in Ref. [29]. We further compare these constraints with those from *Planck* derived both in a Bayesian and a frequentist framework. Note that the

emulator S of Eq. (6) does not span the whole range of Γ and v that we studied for *Planck*. In particular, the best-fit obtained with *Planck* data corresponds to a value of $\log_{10} \Gamma$ slightly above its upper limit in the range of the emulator.

One can see that when we use large priors on n_s and A_s (in blue), we obtain no constraints in the range of parameters spanned by the emulator, while when we use small priors (in yellow) similar to Ref. [29], we exclude a large region of the parameter space corresponding to high values of Γ and v . This behaviour can be understood by looking at the correlation between the spectral index and the plan $\Gamma-v$, depicted in Fig. 6. The coloured bands correspond to isocontours of n_s values. It is clear that Γ and v are strongly correlated with the value of n_s that reaches $1.6 \lesssim n_s$ for models with high Γ and v . This demonstrates that, as anticipated from our discussion of Fig. 4, one can compensate for the effect of a power suppression in the DDM model by adjusting the spectral tilt.

However, it is clear that imposing *Planck* priors on A_s and n_s in the KiDS-1000 analysis can prevent the strong degeneracy that we have uncovered from affecting the resulting constraints on the DDM parameters. We show in Fig. 7 the impact of imposing *Planck* constraints to n_s and A_s as Gaussian priors through the black contours, with values provided in Table II. All the upper right part of the $\Gamma-v$ plan is now consistently excluded. Interestingly, one can identify a region of the parameter space at the intersection of the 1σ confidence level built from *Planck* data and the $1-2\sigma$ constraints from KiDS-1000. This is precisely the region that was found to alleviate the S_8 tension in past studies [24, 29, 77, 78]. As KiDS-1000 data have recently been updated in KiDS-Legacy [8], whether the new data would firmly rule out this region remains to be confirmed. This figure also illustrates the power of multi-probe and multi-scale cosmological analyses: the constraining power of *Planck* at large scales allowed to obtain accurate A_s and n_s constraints, while the constraints from KiDS-1000 at small-scales constrain S_8 and therefore the DDM parameters.

Summarising, our results are nicely illustrated by the combined Bayesian constraints on the matter power spectrum shown from KiDS-1000 with *Planck* priors on A_s and n_s , shown in Fig. 8. One can see that with such priors, the S_8 -kernel does match the best constrained area, although it extends to even smaller scales. In that case, the *Planck* best-fit DDM model appears to be excluded as it predicts a too strong suppression above $k \gtrsim 1 h/\text{Mpc}$. However, constraints to the matter power spectrum relax at scales $\log_{10} k \gtrsim 0.5 h/\text{Mpc}$. This result underscores the constraining power of large-scale structure data beyond the sole S_8 statistic and highlights the importance of consistent, physically motivated priors when combining early- and late-time cosmological observations to constrain DM properties.

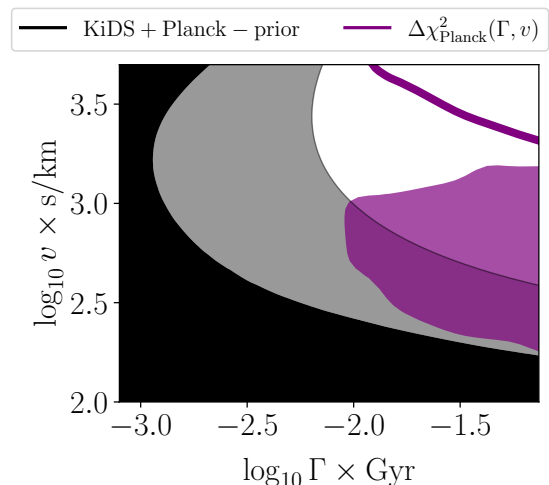


FIG. 7. Constraints on the two additional parameters of the DDM model for *Planck*. The black contour shows the Bayesian KiDS-1000 combined with *Planck* prior on A_s and n_s . The purple contours show the *Planck* profile likelihood result.

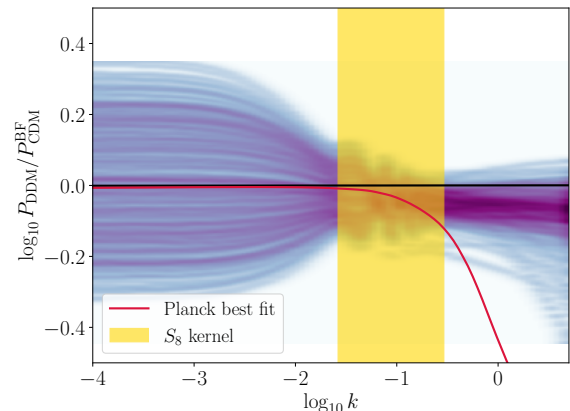


FIG. 8. Bayesian constraints on the matter power spectrum from KiDS-1000 combined with the *Planck* A_s and n_s priors in the DDM model. Like in Fig. 4, the red curve shows the *Planck* maximum likelihood power spectrum with the DDM model, and the yellow band represents the main support of the S_8 kernel defined as $W(8h/\text{Mpc}, k) > 0.1$, see Eq. (2).

V. CONCLUSIONS

We have investigated the two-body Decaying Dark Matter (DDM) model as an extension of the standard cosmological scenario, in which cold dark matter particles decay into a warm daughter particle and a massless dark relativistic particle [24, 41]. This framework introduces two new physical parameters related to the decay dynamics: the decay rate Γ and the momentum transfer v . For sufficiently small values of these parameters, the model reproduces standard ΛCDM predictions at early times, including CMB anisotropies with pure CDM component, while introducing distinctive late-time effects such as a

Dark matter model	CDM		DDM		
	<i>Planck</i>	KiDS-1000	<i>Planck</i>	KiDS-1000	KiDS-1000+ <i>Planck</i> Prior
Ω_m	0.3114 ± 0.0055	$0.233^{+0.031}_{-0.092}$	0.3110 ± 0.0056	$0.226^{+0.040}_{-0.076}$	0.287 ± 0.037
S_8	0.826 ± 0.010	$0.757^{+0.033}_{-0.018}$	$0.816^{+0.022}_{-0.0066}$	$0.755^{+0.037}_{-0.018}$	$0.768^{+0.020}_{-0.018}$
n_s	0.9666 ± 0.0037	$1.05^{+0.11}_{-0.14}$	0.9668 ± 0.0037	$1.05^{+0.10}_{-0.16}$	0.9669 ± 0.0038
$\ln 10^{10} A_s$	3.046 ± 0.014	$3.83^{+1.1}_{-0.81}$	3.045 ± 0.015	3.81 ± 0.79	3.045 ± 0.015
f_{DDM}	n/a	n/a	$<_{2\sigma} -0.16$	$<_{2\sigma} -0.14$	$<_{2\sigma} -1.32$

TABLE II. Constraints at a 68% confidence level (and 95% confidence level for f_{DDM}) on the cosmological parameter of interest. For the DDM model parameters, we provide the combination of the two parameters that is better constrained by the data.

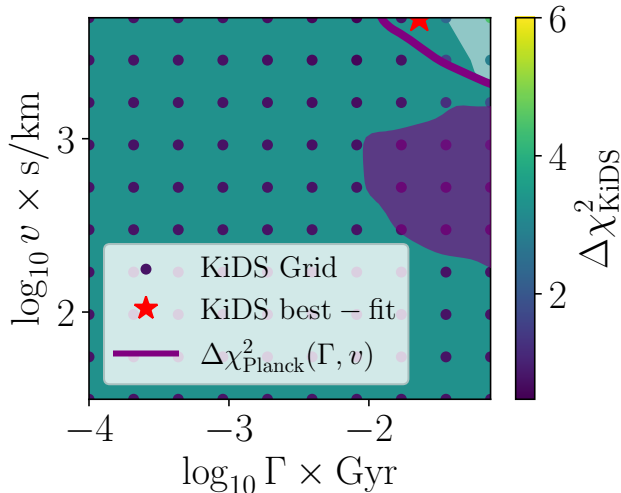


FIG. 9. KiDS-1000 2D profile likelihood for $\Gamma - v$. The grid of DDM parameters used is shown as dots with colours corresponding to the minimum χ^2 over all other parameters. The red star corresponds to the global minimum by also varying $\Gamma - v$ and the purple line shows again the *Planck* 1 and 2σ frequentist confidence level.

time- and scale-dependent suppression of power on small scales. The ability of this model to relax late-time constraints on the properties of dark matter makes it a compelling candidate for addressing tensions in large-scale structure observations. Overall, it allows us to test the stability of dark matter on cosmological time scales, as unstable dark matter candidates naturally arise in many particle physics models [30–36].

Using the matter power spectrum prediction in the linear regime, [24, 49] and nonlinear regime calibrated on simulations [29], we have performed a standard Bayesian analysis of *Planck*-2018 + BOSS-BAO + the Pantheon-Plus supernovae data (referred to as “*Planck*”) on the one hand, and KiDS-1000 data on the other hand, reproducing previous results that suggest a limited ability of the DDM model to alleviate the tension between *Planck* and KiDS-1000 data. However, we have pointed out that the lack of constraints on the new DDM parameters can easily induce large volume prior effects that could alter the consistency of the two datasets.

To bypass this problem, we have performed for the

first time a frequentist analysis of the DDM model in light of *Planck* data. Interestingly, we have found a 68% confidence level that strongly differs from its Bayesian counterparts, with the hint of a slight preference for a specific region of the DDM parameter space that allows to reduce S_8 . This confirms the presence of volume effects in the Bayesian analysis. In fact, we have found that the S_8 value reconstructed in the frequentist analysis is in agreement at 1σ with that of KiDS-1000, with a best-fit that is even lower, $S_8 = 0.70$. At the 95% confidence level, frequentist and Bayesian constraints agree, and volume effects are negligible.

In a second part, we have discussed the constraints set by the different surveys directly at the level of the matter power spectrum in order to better understand the origin of the S_8 tension and its resolution within the DDM model. We have shown that *Planck* data can constrain large scales precisely but allow for significant power suppression precisely in the range of scales probed by KiDS-1000. On the other hand, KiDS-1000 do not allow to significantly constrain large-scales and small-scales independently (in particular A_s and n_s). It only constrains a range of scales close to (but not exactly on) the S_8 kernel. As a result, large degeneracies with the DDM parameters prevent obtaining meaningful constraints on the DDM model in a KiDS-1000 only analysis.

Concretely, we demonstrated that when using broad, uninformative priors, KiDS-1000 data alone do not constrain the DDM parameters (Γ, v) , owing to a degeneracy between the spectral index n_s and (Γ, v) . This sensitivity to the prior volume reveals that previous KiDS-1000 constraints on DDM, such as those from Ref. [29], are significantly influenced by prior choices. We have thus performed a dedicated KiDS-1000 analysis using *Planck*-informed priors on n_s and A_s . While this allows for a significant improvement of the constraints over the results from *Planck* and KiDS-1000 alone, we find that a region of parameter space favoured in the *Planck* frequentist analysis at 68% C.L. does survive the KiDS-1000 constraints. This precisely matches the region that was found to alleviate the tension between both datasets in past studies [24, 29, 77, 78]. It remains to be seen whether the updated KiDS-Legacy or DES-Y3 data that show no tension with *Planck* would firmly exclude this region. Our work demonstrates the importance of combining probes that cover multiple scales to derive robust

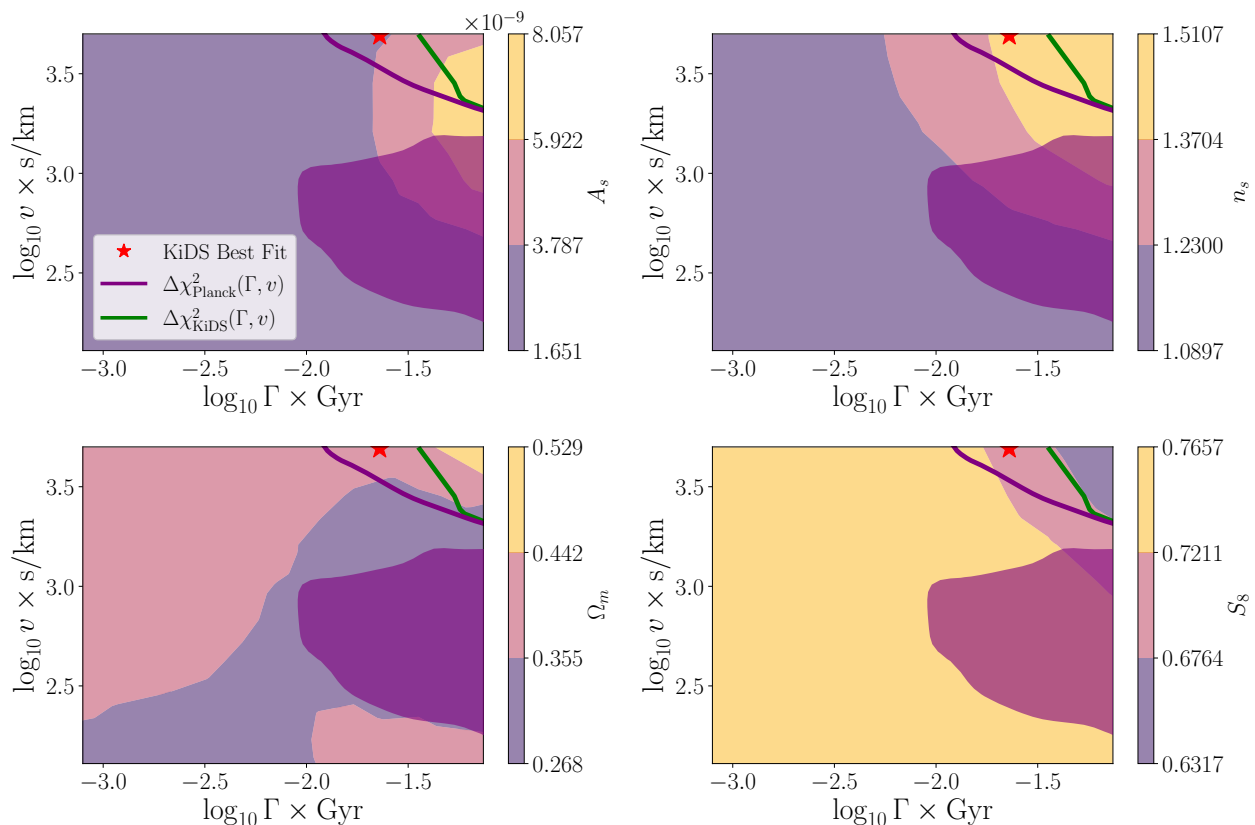


FIG. 10. Isocontours of the best-fit values of A_s , n_s , Ω_m and S_8 obtained when maximising the KiDS-1000 likelihood on the 2D $\Gamma - v$ grid shown in Fig. 9.

constraints on exotic dark matter properties. Looking forward, future weak lensing surveys such as *Euclid* will dramatically improve sensitivity to the scale- and time-dependent suppression of structure induced by DDM models. Recent forecast analyses [79, 80] show that *Euclid* will tighten constraints on the DDM parameter space by up to an order of magnitude, enabling a definitive test of the scenarios discussed in this work.

ACKNOWLEDGMENTS

We thank Théo Simon, Andreas Nygaard, Jozef Bucko, Aurel Schneider and Oliver Hahn for useful discussions. We are particularly thankful to Guillermo Franco Abellán for his thoughtful comments and suggestions on the draft. EMT, TM, AP and VP are supported by funding from the European Research Council (ERC) under the European Union’s HORIZON-ERC-2022 (grant agreement no. 101076865). We gratefully acknowledge support from the CNRS/IN2P3 Computing Center (Lyon - France) for providing computing and data-processing resources needed for this work.

Appendix A: KiDS-1000 Profile Likelihood

We have performed the 2D profile likelihood analysis of the KiDS-1000 data by following the same method as for *Planck*, see Eq. (10). The result is shown in Fig. 9. The global best-fit obtained is indicated as a red star while the colours of the grid points axis correspond to $\Delta\chi_{\text{KiDS}}^2(\Gamma, v)$. In dark and light green, we show respectively the 1 and 2σ confidence level defined as $\Delta\chi_{\text{KiDS}}^2(\Gamma, v) = 2.3$ and $\Delta\chi_{\text{KiDS}}^2(\Gamma, v) = 6.17$. The KiDS-1000 frequentist analysis seems to show that the Bayesian constraints obtained in Ref. [29] and reproduced with small priors on n_s in Fig. 5 is a prior effect.

However, we caution against strongly interpreting these results. Indeed, we find that the preferred value of v tends to the highest value reachable by the emulator $v = 5000$ km/s. At the same time, the redshift dependence of the intrinsic alignment parameter called α_1 in CosmoSIS and η_1 in [55] tends to the highest allowed value by the default prior 5. Unlike all the other nuisance parameters, α_1 only has a flat prior, which appears to make it diverge during the minimisation procedure. Furthermore, the correlation between α_1 and n_s or S_8 is large, which means that $\alpha_1 \rightarrow 5$ can generate very low S_8 values (< 0.70) or large n_s (> 1.2). In Fig. 10 we plot the isocontours for the best-fit parameters A_s , n_s , Ω_m and

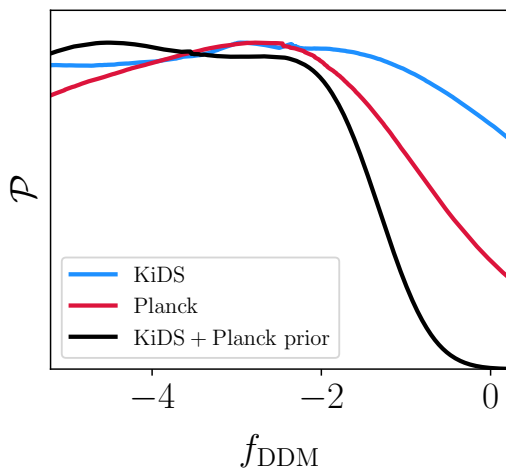


FIG. 11. 1D marginalised constraints on the combination of the two DDM parameters. The left limit of the plot corresponds to a CDM limit. We have improved the constraints by combining KiDS-1000 (in blue) with *Planck* (in red) informed priors on A_s and n_s . The 2σ upper limits are shown in Table II

S_8 . For all these parameters, we observe that the upper right part gives high A_s , n_s and Ω_m , that all together correspond to a very low S_8 value ($S_8 < 0.67$).

Appendix B: Marginalised Statistics

The constraints on DDM can be hard to represent with marginalised 1-dimensional statistics. Indeed, as long as CDM is not excluded, the two strongly correlated parameters Γ and v can take any value as long as the other one is small enough, *i.e.* a large momentum transfer would have no effect if the particle lifetime is much larger than the age of the Universe, while a small lifetime would have no effect if the daughter particle remains cold. For this reason, the marginalised constraints on these parameters depend on the prior, which makes it difficult to interpret and compare between different analyses. As we have seen, *e.g.* Figs. 3 and 7, the data can provide constraints on the combination of Γ and v such that only simultaneously large values can be excluded. Hence, it makes sense to define the effective parameter

$$f_{\text{DDM}} = \log_{10} \left(\frac{\Gamma}{\Gamma_0} \times \frac{v}{v_0} \right), \quad (\text{B1})$$

where Γ_0 and v are arbitrary normalization values. Here, we choose the upper bounds of the emulator $\Gamma_0 = 1/13.5 \text{ Gyr}^{-1}$ and $v_0 = 5000 \text{ km/s}$. Effectively, when $f_{\text{DDM}} \ll 0$, we recover the CDM limit either by large lifetime or small momentum transfer. Constraints to this DDM parameter are shown in Fig. 11. One can see that the combination of KiDS-1000 and *Planck* priors provide the strongest constraints to the model.

Finally, in Tab. II, we show the 1-dimensional marginalised constraints for all parameters, the two models we have considered, CDM and DDM, and the two datasets we have used *Planck* and KiDS-1000. The last column shows the combination of KiDS-1000 and *Planck* informed priors on A_s and n_s .

-
- [1] N. Aghanim *et al.* (Planck), *Astron. Astrophys.* **641**, A6 (2020), [Erratum: *Astron. Astrophys.* 652, C4 (2021)], [arXiv:1807.06209 \[astro-ph.CO\]](#).
- [2] K. Kuijken *et al.*, *Astron. Astrophys.* **625**, A2 (2019), [arXiv:1902.11265 \[astro-ph.GA\]](#).
- [3] B. Giblin *et al.*, *Astron. Astrophys.* **645**, A105 (2021), [arXiv:2007.01845 \[astro-ph.CO\]](#).
- [4] A. Amon *et al.* (DES), *Phys. Rev. D* **105**, 023514 (2022), [arXiv:2105.13543 \[astro-ph.CO\]](#).
- [5] T. Hamana *et al.*, *Publ. Astron. Soc. Jap.* **72**, 16 (2020), [Erratum: *Publ. Astron. Soc. Jap.* 74, 488-491 (2022)], [arXiv:1906.06041 \[astro-ph.CO\]](#).
- [6] J. L. v. d. Busch *et al.*, *Astron. Astrophys.* **664**, A170 (2022), [arXiv:2204.02396 \[astro-ph.CO\]](#).
- [7] T. M. C. Abbott *et al.* (DES), *Phys. Rev. D* **105**, 023520 (2022), [arXiv:2105.13549 \[astro-ph.CO\]](#).
- [8] B. Stölzner *et al.*, (2025), [arXiv:2503.19442 \[astro-ph.CO\]](#).
- [9] v. Ivezić *et al.* (LSST), *Astrophys. J.* **873**, 111 (2019), [arXiv:0805.2366 \[astro-ph\]](#).
- [10] Y. Mellier *et al.* (Euclid), *Astron. Astrophys.* **697**, A1 (2025), [arXiv:2405.13491 \[astro-ph.CO\]](#).
- [11] D. Spergel *et al.*, (2015), [arXiv:1503.03757 \[astro-ph.IM\]](#).
- [12] Y. Gong, X. Liu, Y. Cao, X. Chen, Z. Fan, R. Li, X.-D. Li, Z. Li, X. Zhang, and H. Zhan, *Astrophys. J.* **883**, 203 (2019), [arXiv:1901.04634 \[astro-ph.CO\]](#).
- [13] T. Tan, D. Zuercher, J. Fluri, A. Refregier, F. Tarsitano, and T. Kacprzak, *Mon. Not. Roy. Astron. Soc.* **522**, 3766 (2023), [arXiv:2207.03598 \[astro-ph.CO\]](#).
- [14] A. Amon and G. Efstathiou, *Mon. Not. Roy. Astron. Soc.* **516**, 5355 (2022), [arXiv:2206.11794 \[astro-ph.CO\]](#).
- [15] G. Aricò, R. E. Angulo, M. Zennaro, S. Contreras, A. Chen, and C. Hernández-Monteagudo, *Astron. Astrophys.* **678**, A109 (2023), [arXiv:2303.05537 \[astro-ph.CO\]](#).
- [16] A. Schneider, A. Refregier, S. Grandis, D. Eckert, N. Stoira, T. Kacprzak, M. Knabenhans, J. Stadel, and R. Teyssier, *JCAP* **04**, 020 (2020), [arXiv:1911.08494 \[astro-ph.CO\]](#).
- [17] S. Heimersheim, N. Schöneberg, D. C. Hooper, and J. Lesgourgues, *JCAP* **12**, 016 (2020), [arXiv:2008.08486 \[astro-ph.CO\]](#).
- [18] M. Joseph, D. Aloni, M. Schmaltz, E. N. Sivarajan,

- and N. Weiner, *Phys. Rev. D* **108**, 023520 (2023), [arXiv:2207.03500 \[astro-ph.CO\]](#).
- [19] V. Poulin, J. L. Bernal, E. D. Kovetz, and M. Kamionkowski, *Phys. Rev. D* **107**, 123538 (2023), [arXiv:2209.06217 \[astro-ph.CO\]](#).
- [20] F. Ferlito, S. Vagnozzi, D. F. Mota, and M. Baldi, *Mon. Not. Roy. Astron. Soc.* **512**, 1885 (2022), [arXiv:2201.04528 \[astro-ph.CO\]](#).
- [21] K. Enqvist, S. Nadathur, T. Sekiguchi, and T. Takahashi, *JCAP* **09**, 067 (2015), [arXiv:1505.05511 \[astro-ph.CO\]](#).
- [22] K. Enqvist, S. Nadathur, T. Sekiguchi, and T. Takahashi, *JCAP* **04**, 015 (2020), [arXiv:1906.09112 \[astro-ph.CO\]](#).
- [23] R. Murgia, A. Merle, M. Viel, M. Totzauer, and A. Schneider, *JCAP* **11**, 046 (2017), [arXiv:1704.07838 \[astro-ph.CO\]](#).
- [24] G. Franco Abellán, R. Murgia, and V. Poulin, *Phys. Rev. D* **104**, 123533 (2021), [arXiv:2102.12498 \[astro-ph.CO\]](#).
- [25] A. Chen *et al.* (DES), *Phys. Rev. D* **103**, 123528 (2021), [arXiv:2011.04606 \[astro-ph.CO\]](#).
- [26] G. Choi and T. T. Yanagida, *Phys. Lett. B* **827**, 136954 (2022), [arXiv:2104.02958 \[hep-ph\]](#).
- [27] H. Tanimura, M. Douspis, N. Aghanim, and J. Kuruvilla, *Astron. Astrophys.* **674**, A222 (2023), [arXiv:2301.03939 \[astro-ph.CO\]](#).
- [28] J. Bucko, S. K. Giri, and A. Schneider, *Astron. Astrophys.* **672**, A157 (2023), [arXiv:2211.14334 \[astro-ph.CO\]](#).
- [29] J. Bucko, S. K. Giri, F. H. Peters, and A. Schneider, *Astron. Astrophys.* **683**, A152 (2024), [arXiv:2307.03222 \[astro-ph.CO\]](#).
- [30] T. Hambye, *PoS IDM2010*, 098 (2011), [arXiv:1012.4587 \[hep-ph\]](#).
- [31] K. N. Abazajian *et al.*, (2012), [arXiv:1204.5379 \[hep-ph\]](#).
- [32] M. Drewes *et al.*, *JCAP* **01**, 025 (2017), [arXiv:1602.04816 \[hep-ph\]](#).
- [33] V. Berezhinsky, A. Masiero, and J. W. F. Valle, *Phys. Lett. B* **266**, 382 (1991).
- [34] L. Covi, J. E. Kim, and L. Roszkowski, *Phys. Rev. Lett.* **82**, 4180 (1999), [arXiv:hep-ph/9905212](#).
- [35] H.-B. Kim and J. E. Kim, *Phys. Lett. B* **527**, 18 (2002), [arXiv:hep-ph/0108101](#).
- [36] J. L. Feng, A. Rajaraman, and F. Takayama, *Phys. Rev. D* **68**, 063504 (2003), [arXiv:hep-ph/0306024](#).
- [37] L. Fuß, M. Garny, and A. Ibarra, *JCAP* **01**, 055 (2025), [arXiv:2403.15543 \[hep-ph\]](#).
- [38] A. Nygaard, T. Tram, and S. Hannestad, *JCAP* **05**, 017 (2021), [arXiv:2011.01632 \[astro-ph.CO\]](#).
- [39] E. B. Holm, L. Herold, S. Hannestad, A. Nygaard, and T. Tram, *Phys. Rev. D* **107**, L021303 (2023), [arXiv:2211.01935 \[astro-ph.CO\]](#).
- [40] T. Simon, G. Franco Abellán, P. Du, V. Poulin, and Y. Tsai, *Phys. Rev. D* **106**, 023516 (2022), [arXiv:2203.07440 \[astro-ph.CO\]](#).
- [41] M.-Y. Wang and A. R. Zentner, *Phys. Rev. D* **85**, 043514 (2012), [arXiv:1201.2426 \[astro-ph.CO\]](#).
- [42] A. H. G. Peter and A. J. Benson, *Phys. Rev. D* **82**, 123521 (2010), [arXiv:1009.1912 \[astro-ph.GA\]](#).
- [43] D. Cheng, M. C. Chu, and J. Tang, *JCAP* **07**, 009 (2015), [arXiv:1503.05682 \[astro-ph.CO\]](#).
- [44] S. Mau *et al.* (DES), *Astrophys. J.* **932**, 128 (2022), [arXiv:2201.11740 \[astro-ph.CO\]](#).
- [45] M.-Y. Wang, R. A. C. Croft, A. H. G. Peter, A. R. Zentner, and C. W. Purcell, *Phys. Rev. D* **88**, 123515 (2013), [arXiv:1309.7354 \[astro-ph.CO\]](#).
- [46] L. Fuß and M. Garny, *JCAP* **10**, 020 (2023), [arXiv:2210.06117 \[astro-ph.CO\]](#).
- [47] A. Nygaard, E. B. Holm, S. Hannestad, and T. Tram, *JCAP* **11**, 064 (2023), [arXiv:2308.06379 \[astro-ph.CO\]](#).
- [48] D. J. Fixsen, *Astrophys. J.* **707**, 916 (2009), [arXiv:0911.1955 \[astro-ph.CO\]](#).
- [49] G. Blackadder and S. M. Koushiappas, *Phys. Rev. D* **90**, 103527 (2014), [arXiv:1410.0683 \[astro-ph.CO\]](#).
- [50] J. Lesgourgues, (2011), [arXiv:1104.2932 \[astro-ph.IM\]](#).
- [51] D. Blas, J. Lesgourgues, and T. Tram, *JCAP* **07**, 034 (2011), [arXiv:1104.2933 \[astro-ph.CO\]](#).
- [52] R. Takahashi, M. Sato, T. Nishimichi, A. Taruya, and M. Oguri, *Astrophys. J.* **761**, 152 (2012), [arXiv:1208.2701 \[astro-ph.CO\]](#).
- [53] R. E. Smith, J. A. Peacock, A. Jenkins, S. D. M. White, C. S. Frenk, F. R. Pearce, P. A. Thomas, G. Efstathiou, and H. M. P. Couchmann (VIRGO Consortium), *Mon. Not. Roy. Astron. Soc.* **341**, 1311 (2003), [arXiv:astro-ph/0207664](#).
- [54] S. K. Giri and A. Schneider, *JCAP* **12**, 046 (2021), [arXiv:2108.08863 \[astro-ph.CO\]](#).
- [55] T. M. C. Abbott *et al.* (Kilo-Degree Survey, DES), *Open J. Astrophys.* **6**, 2305.17173 (2023), [arXiv:2305.17173 \[astro-ph.CO\]](#).
- [56] A. Mead, S. Brieden, T. Tröster, and C. Heymans, *Mon. Not. Roy. Astron. Soc.* **502**, 1401 (2021), [arXiv:2009.01858 \[astro-ph.CO\]](#).
- [57] M. Asgari *et al.* (KiDS), *Astron. Astrophys.* **645**, A104 (2021), [arXiv:2007.15633 \[astro-ph.CO\]](#).
- [58] B. Joachimi *et al.*, *Astron. Astrophys.* **646**, A129 (2021), [arXiv:2007.01844 \[astro-ph.CO\]](#).
- [59] N. Aghanim *et al.* (Planck), *Astron. Astrophys.* **641**, A5 (2020), [arXiv:1907.12875 \[astro-ph.CO\]](#).
- [60] N. Aghanim *et al.* (Planck), *Astron. Astrophys.* **641**, A8 (2020), [arXiv:1807.06210 \[astro-ph.CO\]](#).
- [61] F. Beutler, C. Blake, M. Colless, D. H. Jones, L. Staveley-Smith, L. Campbell, Q. Parker, W. Saunders, and F. Watson, *Mon. Not. Roy. Astron. Soc.* **416**, 3017 (2011), [arXiv:1106.3366 \[astro-ph.CO\]](#).
- [62] A. J. Ross, L. Samushia, C. Howlett, W. J. Percival, A. Burden, and M. Manera, *Mon. Not. Roy. Astron. Soc.* **449**, 835 (2015), [arXiv:1409.3242 \[astro-ph.CO\]](#).
- [63] S. Alam *et al.* (BOSS), *Mon. Not. Roy. Astron. Soc.* **470**, 2617 (2017), [arXiv:1607.03155 \[astro-ph.CO\]](#).
- [64] D. Brout *et al.*, *Astrophys. J.* **938**, 110 (2022), [arXiv:2202.04077 \[astro-ph.CO\]](#).
- [65] P. Schneider, T. Eifler, and E. Krause, *Astron. Astrophys.* **520**, A116 (2010), [arXiv:1002.2136 \[astro-ph.CO\]](#).
- [66] M. Asgari, P. Schneider, and P. Simon, *Astron. Astrophys.* **542**, A122 (2012), [arXiv:1201.2669 \[astro-ph.CO\]](#).
- [67] M. Asgari, C. Heymans, C. Blake, J. Harnois-Deraps, P. Schneider, and L. Van Waerbeke, *Mon. Not. Roy. Astron. Soc.* **464**, 1676 (2017), [arXiv:1601.00115 \[astro-ph.CO\]](#).
- [68] N. Metropolis, A. W. Rosenbluth, M. N. Rosenbluth, A. H. Teller, and E. Teller, *J. Chem. Phys.* **21**, 1087 (1953).
- [69] W. K. Hastings, *Biometrika* **57**, 97 (1970).
- [70] T. Brinckmann and J. Lesgourgues, *Phys. Dark Univ.* **24**, 100260 (2019), [arXiv:1804.07261 \[astro-ph.CO\]](#).
- [71] B. Audren, J. Lesgourgues, K. Benabed, and S. Prunet, *JCAP* **02**, 001 (2013), [arXiv:1210.7183 \[astro-ph.CO\]](#).
- [72] J. Zuntz, M. Paterno, E. Jennings, D. Rudd, A. Man-

- zotti, S. Dodelson, S. Bridle, S. Sehrish, and J. Kowalkowski, *Astron. Comput.* **12**, 45 (2015), [arXiv:1409.3409 \[astro-ph.CO\]](#).
- [73] S. Hannestad, *Phys. Rev. D* **61**, 023002 (2000), [arXiv:astro-ph/9911330](#).
- [74] A. H. Wright *et al.*, (2025), [arXiv:2503.19441 \[astro-ph.CO\]](#).
- [75] C. Heymans *et al.*, *Astron. Astrophys.* **646**, A140 (2021), [arXiv:2007.15632 \[astro-ph.CO\]](#).
- [76] J. Neyman, *Phil. Trans. Roy. Soc. Lond. A* **236**, 333 (1937).
- [77] G. Franco Abellán, R. Murgia, V. Poulin, and J. Lavalley, *Phys. Rev. D* **105**, 063525 (2022), [arXiv:2008.09615 \[astro-ph.CO\]](#).
- [78] T. Simon, P. Zhang, V. Poulin, and T. L. Smith, *Phys. Rev. D* **107**, 063505 (2023), [arXiv:2208.05930 \[astro-ph.CO\]](#).
- [79] J. Lesgourgues *et al.* (Euclid), *Astron. Astrophys.* **693**, A249 (2025), [arXiv:2406.18274 \[astro-ph.CO\]](#).
- [80] G. Franco Abellán, G. C. n. Herrera, M. Martinelli, O. Savchenko, D. Sciotti, and C. Weniger, *JCAP* **11**, 057 (2024), [arXiv:2403.14750 \[astro-ph.CO\]](#).